Infiltration studies of additive manufacture of WC with Co using binder jetting and pressureless melt method

Corson L. Cramer[1,*], Peeyush Nandwana[2], Richard A. Lowden[2], Amy M. Elliott[1]

[1]Energy & Transportation Science Division, Energy and Environmental Sciences Directorate,

Oak Ridge National Laboratory, Oak Ridge, TN, USA

[2]Materials Science and Technology Division, Physical Sciences Directorate, Oak Ridge National

Laboratory, Oak Ridge, TN, USA

*cramercl@ornl.gov

Abstract

Additive manufacturing (AM) of tungsten carbide-cobalt (WC-Co) is explored starting with WC preforms shaped with binder jet additive manufacturing (BJAM) followed by melt infiltration of Co. The research objective is to demonstrate the ability to net-shape WC-Co composites through BJAM of a WC preform followed by backfilling with cobalt via pressureless infiltration. This method also has the potential to minimize shrinkage and grain growth compared to other AM techniques. The effects of sintering, Co content, and infiltration time on the net shaping and properties of processed composites are shown. The best shaped material had an average grain size of 5.1 μm, 32 vol.% Co, density of 98.54% theoretical, fracture toughness of 23.2 $MPa \cdot m^{1/2}$, and hardness of 9.0 GPa. Data presented illustrates that the proposed approach results in favorable ceramic-metal (cermet) properties and is viable for fabricating cermets of other material combinations. Successful AM of cermets provides complex geometries, high throughout, and low costs.

Keywords: Binder jet additive manufacturing, cermet composite, Pressureless melt infiltration

Introduction

Tungsten carbide-cobalt (WC-Co) is a ceramic-metal (cermet) or ceramic composite structure [1] that is highly useful for cutting tools and mining bits due to the combined hardness and fracture toughness [2]. Ceramic-metal (cermet) structures like WC-Co are typically processed with casting and powder metallurgy techniques, but additive manufacturing (AM) can improve the geometric complexity and throughput with no tooling costs. Therefore, the net-shaping of this material system with AM is explored. Specifically, binder jet additive manufacturing (BJAM) followed by melt infiltration can provide a near-net shape with minimal shrinkage and less grain growth because the porosity of the WC preform is backfilled with liquid Co and time at temperature can be reduced, so it is advantageous compared to sintering of composite powder. Ultimately, developing the BJAM and melt infiltration process settings with WC-Co can provide insight to fabricating WC-Co and other cermet materials through AM with minimal shrinkage and comparable properties.

Cornwall and German discussed how WC-Co has been used widely in industry for cutting tools, mining bits, and armor penetrators since its advent in 1923 in Germany because it retains both high hardness and high fracture toughness even at elevated temperatures [3]. Specifically, Ettmayer defines the useful range of Co content in WC-Co cermets of 5-25wt.% (corresponding to 8.5-37vol.%), giving the material superior hardness, compressive strength, fracture toughness, and transverse rupture strength [4]. Also, Gurland and Norton showed that WC-Co provides excellent wear properties [2]. Furthermore, the manufacturing of WC-Co materials has been done with dry-pressed parts by mixing, milling, sand casting, and liquid-phase sintering of the two materials [5]. Injection molding of WC-Co was performed with good shape retention and minimal shrinkage, but drawbacks exist in the process such as the cost of tooling and eta (η) phase formation [6]. Scheithauer achieved additive manufacturing of WC-Co with limited porosity by extrusion of thermoplastic binder loaded with WC-Co powder, but the shrinkage is not reported from a 67 vol.% solid-loaded slurry that was sintered, and there is no elemental analysis reported [7]. Also, WC-Co parts were formed by slurry-based three-dimensional printing (3DPTM) method using WC and cobalt oxide precursor and achieved net-shaping with some shrinkage and high density [8]. Despite molding and extruding of WC-Co with good shape retention and minimal shrinkage, more complex geometries are achievable with 3-d printing shaping technology, and controlled geometry is highly achievable with selective laser melting (SLM) and selective laser sintering (SLS) [9], [10]. There is a potential issue with cracking of the material and producing η-phase when using SLM and SLS [11], [12], so a possible, alternate technique for shaping powder is sought with BJAM, which is also more cost effective and provides higher throughput [13].

BJAM is a powder-based additive manufacturing technique that uses polymer in a solvent to bind powders together in a powder bed on a micron-sized layer scale [14]. BJAM starts with a CAD file that is sliced into layers in an STL file. The layers are built upward in the powder bed starting with a thin distribution of powder spread over the surface of the powder bed. In a process like ink-jet printing, a binder, consisting of polymer and solvent, is jetted onto the powder bed in the 2-dimensional slice from the STL file to join particles where the object is to be formed. A hopper moves over the print area, so the next powder layer can be spread and selectively joined. This layer-by-layer process repeats until the part is completed. After a curing treatment, unbound powder is brushed off and vacuumed away and the printed powder part is removed for sintering or infiltration. BJAM can produce parts with complex geometries with higher throughput while recycling most of the unused material, and this is especially important for processing WC-Co to lower costs.

Enneti et al. used BJAM to process WC-12 wt.% Co starting with printing of composite powder and subsequent liquid-phase sintering and hot isostatic pressing (HIP), but the shrinkage is about 20-25% in all three dimensions because the green part starts at 42% theoretical density (TD) and is processed with sintering and hot isostatic pressing to 94%TD [15]. The downside to the current BJAM process for creating composites such as WC-Co parts is that they require a total volume change of at least 35% from printed to fully consolidated and require long post-processing such as liquid phase sintering and HIP, which increase the grain size and contribute to shrinkage and distortion. Another method for making composites with BJAM is to print the reinforcement material and perform pressureless melt infiltration of matrix material because shrinkage and distortion can be mitigated because the infiltrating metal wicks into the preform and fills the

porosity without traditional particle sintering. Pressureless melt infiltration also limits grain growth because the molten material wets and penetrates on a time scale that is not favorable for grain growth. It has been shown that BJAM and melt infiltration results in fully dense, near-net shaped steel and bronze composites with limited grain growth [16], [17]. WC infiltrated with Co is lacking in the literature, but Co wets WC very well [18] and other materials have infiltrated into WC forming composites [19].

In this paper, BJAM is used to shape WC preforms subsequently pressureless melt infiltrated with Co to minimize the shrinkage and grain growth of the processed WC-Co composite. Printing of WC preforms was conducted and the effects of WC preform sintering, volume fraction of Co used for infiltration, and infiltration time on the net-shaping, bulk properties, and microstructure are explored. These studies are an important step for developing and fabricating WC-Co and other cermets with high density with minimal shrinkage and grain size.

Materials and Methods

Materials

Stoichiometric WC powder from Micron Metals Inc. (WC-302, 99.9% purity, -325 mesh particle size) was processed as-received. The particle size distribution as measured with a Horiba LA-950 particle analyzer using laser scattering of dry powders with a volume distribution and particle percentage. Scanning Electron Microscopy (SEM) and Horiba laser scatter particle distribution analysis are performed on the powder to show the morphology, size, and distribution of the WC powder. Cobalt (99.9% purity) was obtained from American Elements in the form of pellets of 3 mm height x 3 mm diameter for infiltration purposes. The ExOne commercial binder (ProMetal R-1) was used for binding all printed parts.

Processing

WC preforms were printed using an ExOne X1-Lab machine with a solvent-based binder. The feed powder to layer ratio was 1.5:1. Each printed layer was 100 μm, and it was not necessary to change the layer thickness because of the large size distribution of the powder and the sufficient layer to layer connections achieved during printing. The powder spread velocity was 0.5 mm/s, and binder saturation and powder packing were 80% and 40%, respectively. The dry time for each layer was 40 sec. Following printing, the specimens were cured at 200°C in air to allow for drying of the binder, which provides strength to the green part. The printed parts were recovered from the powder bed after curing was completed. A cuboid shape of $15 \times 15 \times 5$ mm was selected for the printed WC preform so that three axes of dimensions could be measured throughout processing.

After printing, the resulting green parts were processed in an Inconel tube furnace to "de-bind" or burn off the polymer binder. Debinding in an Inconel tube furnace allows for easier clean up, less reacting, and longer lifetime usage compared to an alumina tube furnace. The temperature for the de-bind cycle was ramped at 5°C/min to 630°C, held at 630°C for 1 h, then ramped to 900°C at 10°C/min, and held for 1 h while flowing gas consisting of 96% Ar and 4% H_2 continuously at 300 cubic centimeters per minute (ccm). According to [20], 630°C is the temperature at which the binder will decompose and leave the green part in gaseous form leaving carbon residue, and the extra step at 900°C is to make sure the binder has is mostly gone; however, it usually leaves behind some carbon residue. The parts were then sintered in an alumina tube furnace to encourage necking

and consolidation of the WC preform. The heating schedule for this sintering step was a temperature ramp at 10°C/min to 1600°C, held for 4 h while flowing 300 ccm of gas consisting of 96% Ar and 4% H_2. Sintering of the WC preform was done to increase preform density and strength, and the resulting dimensional changes were measured for each specimen using calipers. Some preforms were left un-sintered to test the effects of sintering on infiltration.

To determine how much Co infiltrant was needed to fill the voids in the porous WC preform and test varying volume percent of Co, the amount of void space in the porous WC preform was estimated from geometric density. The amount of Co infiltrated was then estimated based on two levels, exact and lean. Exact amount of Co is the estimated void space from pores in the WC preform. The lean amount of Co is an amount less than the estimated void space in the WC preform. The lean amount of Co was arbitrarily chosen to be 50 wt.% less Co than the exact amount. The two levels of Co were used to explore the effects of Co amount on the shrinkage, dissolution, and properties of WC-Co composites processed with infiltration.

After sintering and measuring for infiltrant amount, the infiltration with cobalt occurred in the same tube furnace in a separate cycle. The setup is described. WC preforms rested on top of cobalt pellets in the configuration shown in Fig. 1A. The whole system was heated to 1520°C at 10°C/min, and the Co melts and simultaneously wicks into the WC and starts to spread under the WC preform as in Fig. 1B. This results in further wicking of Co into the WC preform and the lowering of the WC perform to the crucible bottom surface as in Fig. 1C. After cooling, the WC-Co composites rests in the bottom of the crucible as in Fig. 1D. The hold times for processing are either 1 min or 60 min. The composites starting with sintered preforms were held for either 1 min or 60 min at temperature while composites starting with un-sintered preforms were held for 1 min at temperature. To decouple any sintering and infiltration shrinkage that may happen with un-sintered samples, un-sintered samples are run through the same heat schedule as the infiltration heating schedule. The composites were prepared via metallography techniques and analyzed for the effects of sintering, amount of cobalt infiltrant, and processing time on the microstructure.

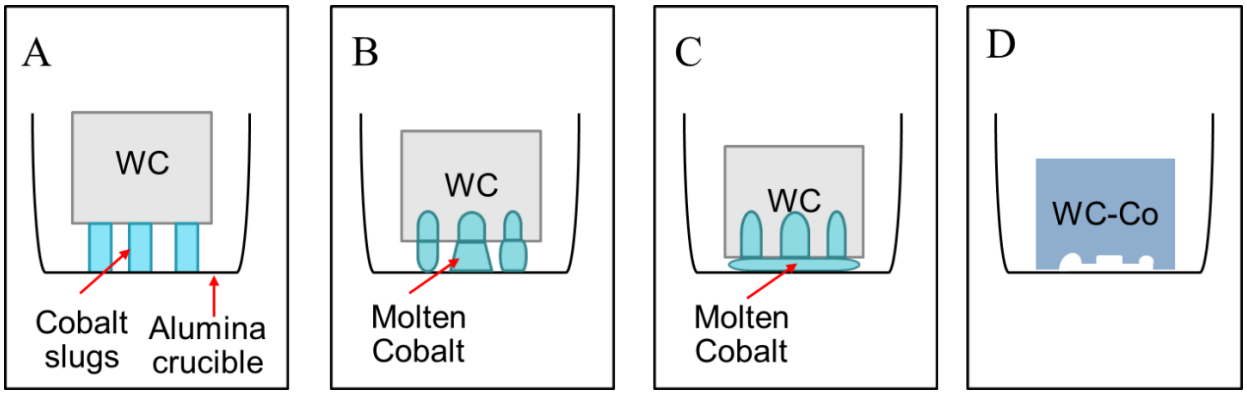

Figure 1: Set up and progression of infiltration of WC with cobalt.

Characterization

The specimen microstructures were analyzed with SEM using a Hitachi S4800 microscope in secondary electron imaging mode after different stages of the process: preform printing, de-binding, sintering, and cobalt infiltration. The densities and geometric changes were also noted at

each step. Geometric, Archimedes, and areal densities were measured when appropriate. Geometric and Archimedes densities were measured by measuring the part dimensions, dry mass, and submerged mass. Areal density was measured using ImageJ software on SEM cross-sections using greyscale threshold. Optical images were taken using a Leica DM4000 M LED system where stitching is used to image full cross-sections. Phase composition was determined by X-ray diffraction (XRD) using a PANalytical X'pert diffractometer with Mo K-α radiation (λ=0.709319 Å). The operating parameters were 40 kV and 40 mA, with a 2θ step size of 0.02. The XRD patterns were analyzed using the whole pattern fitting approach with MDI Jade 2010 software database. Vickers hardness measurements were performed using a LECO LM 110AT apparatus under a 0.5 kgf load. Fracture toughness was measured on samples with the lowest vol.% of Co using this method [21]. Beams of 4 x 4 x 20 mm and notch size of 0.5 mm were placed in 4-point bending fixture, and a crosshead displacement rate of 0.1 mm/min was used with an Instron 8501. Further, the grain size was measured with ASTM E112 using cross-sectional SEM images of flat surfaces with ample statistics and a correction factor of 1.56 for log mean distribution. Specific surface area of the WC powder was calculated using a Brunauer–Emmett–Teller (BET) Quantachrome 2.0 system to aid in dissolution kinetic calculations. Chemical analysis on the as received powder and as printed and debinded powder were done by measuring carbon with ASTM 1941-16 and all other elements with ASTM E 1097-12.

Results

Powder, Printing, and Sintering of WC Preforms

Fig. 2 shows an SEM image of the WC powder and Horiba volume distribution and particle percentage data. The particle size distribution has a D_{50} of 19.21 microns, D_{10} and D_{90} of 10.46 microns and 32.98 microns, respectively. The morphology of the powder is mostly irregular with some particles having spherical shapes.

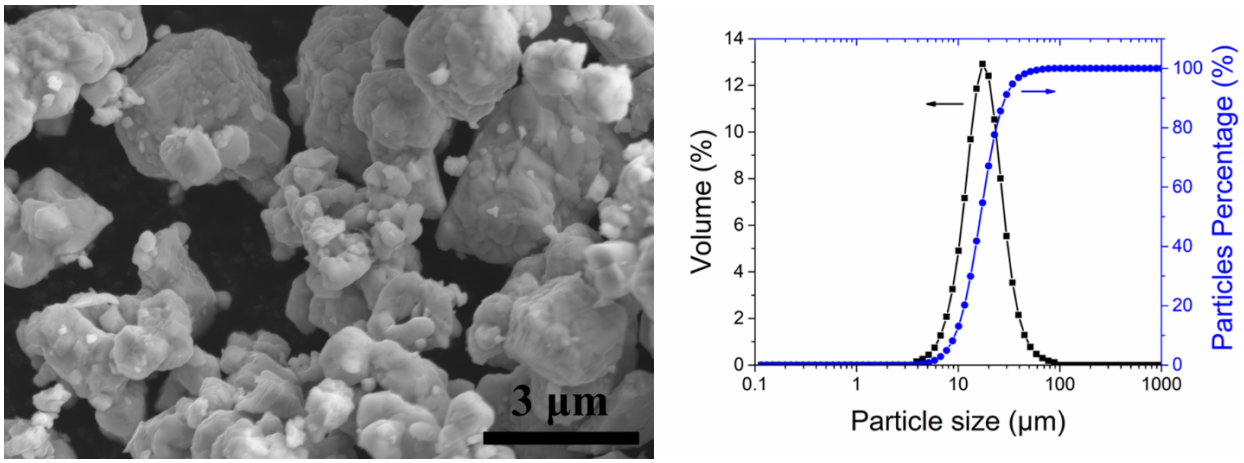

Figure 2: SEM image of WC powder on left and Horiba data on right.

Fig. 3 shows macro images of printed, de-binded, and sintered WC cuboid preforms. There are parallel lines across the tops of the printed preforms from the printhead corresponding to the print direction. The green parts were very fragile, so parts were moved with forceps and placed on foam for transporting to sintering furnaces. The fragility of the green parts also requires delicate handling during measurements with handheld calipers, and the effect of this is considered in the accuracy

of the reported dimensions. While little to no dimensional change nor microstructural difference was observed from after printing to de-binding, the WC preform density increased by 15% after sintering with linear dimensional shrinkage around 10%, as shown in Table 1. The dimensional change in percent in the x-,y-, and z-direction are 10, 11, and 11%, respectively.

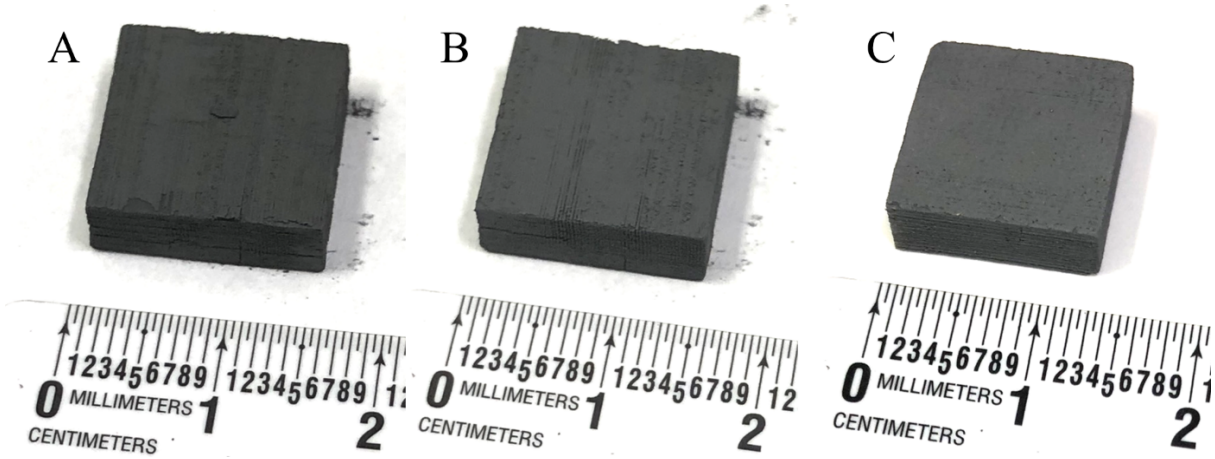

Figure 3: Macro images of A) printed WC, B) de-binded WC, and C) sintered WC preforms.

Table 1: Measured geometric properties of WC preforms after each preform step.

	Printed WC	Printed and De-binded WC	Printed, De-binded, and Sintered WC
Approximate Dimensions (mm)	15±0.1 × 15±0.1 × 5±0.1	15±0.1 × 15±0.1 × 5±0.1	13.4±0.1 × 13.5±0.1 × 4.4±0.1
Approximate Geometric Density (%TD)	33±1	35±1	50±2
Dimensional Change (Δl_1, Δl_2, Δh) (%)	n/a	n/a	10, 11, 11

Fig. 4 shows SEM images of cross sections of a fracture surface of as printed and sintered WC specimens. Fig. 4a and 4b show the print layer lines in the as printed and sintered WC preforms, respectively. The layers are adhered well in the print and remain adhered well during sintering showing that the sintering is uniform in all directions. Fig. 4c and 4d show the morphology of the as printed and sintered WC preform, respectively. During sintering, there is grain growth as well as necking consolidation as evident in the images where rounded pores were observed and satellite particles seem to be one larger particles. This sintering and consolidation step lead to higher strength preforms and higher contiguity of WC after Co infiltration.

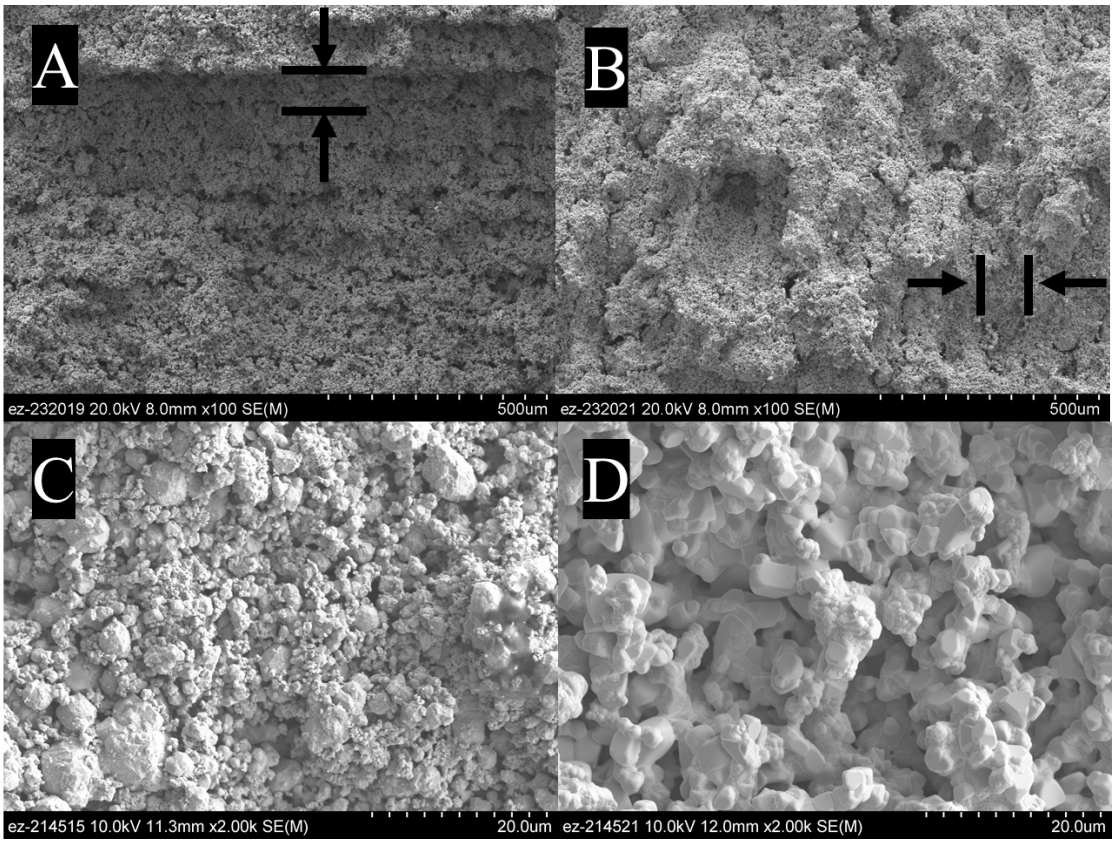

Figure 4: SEM images of layers of cross sections of WC preforms A) after printing B) after sintering and SEM images of morphology of WC preforms C) after printing D) after sintering.

Carbon content is important for the binder jetting process because the polymers typically leave behind carbon during burnout, and this affects sintering and infiltration. Table 2 shows the elemental analysis of the WC power before processing the powder and after the powder has been printed and polymer binder has been burned out to measure the carbon left behind by the binder. It is shown that the ExOne binder leaves behind roughly 0.2 wt.% carbon after burnout in Ar/4%H_2 gas.

Table 2: Elemental analysis showing the wt.% of each element of the WC powder and the printed plus debinded WC samples.

Element	Powder (as received)	Printed and debinded powder
W	93.9	93.7
C	6.04	6.26
Co	<0.01	<0.01
Cr	0.010	0.023
Fe	0.046	0.083
V	<0.01	<0.01
Si	<0.01	0.013

Calculation of Theoretical Properties for Infiltration

Sintered and un-sintered preforms were infiltrated with cobalt in two different amounts relative to the calculated void space in the porous WC preform. As previously mentioned, an "exact" amount of infiltrant used corresponds to the volume of infiltrant required to fill the calculated void space, and the "lean" amount of infiltrant corresponds to an amount of Co that is 50 wt.% less Co from the exact amount. Also, the amount of sintering determines the WC preform density, which determines the amount of Co that corresponds to the approximated "exact" void space in the WC preforms. This means that the exact amount of Co is different for sintered and un-sintered specimens. The calculation for determining the exact amount of Co for infiltration is shown in Eq. (1), where m is the mass, ρ is the density, l_1 is the first length, l_2 is the second length, and h is the height.

$$m_{Co,\,exact} = \frac{\rho_{WC\ preform}}{\rho_{WC,\ theo.}} \cdot (l_{1,\,WC\ preform}\ x\ l_{2,WC\ preform}\ x\ h_{WC\ preform}) \cdot \rho_{Co,\,theo.} \qquad (1)$$

Once infiltrated, a composite is formed with either exact or lean amounts of Co. The theoretically calculated composite densities based on the rule of mixtures are shown below in Table 3 where five samples are measured and standard deviation is calculated. Here, the theoretical values are presented so that they can be compared to the actual processed composites later, and the effects of sintering and Co vol.% are observed. The vol.% Co for specimens processed with lean Co represent the result if the WC and Co completely mix, testing the hypothesis of having a portion of the WC that is un-infiltrated. The WC preform infiltrated with lean amount of Co should have a portion of its volume that is un-infiltrated, or the WC should have vast shrinkage. The lowest vol.% tested is 35 vol.% Co with the sintered and lean specimen, and the highest vol.% Co tested is the un-sintered and exact specimen with 66 vol.% Co.

Table 3: Calculated volume percent of cobalt and theoretical composite densities from preform mass and cobalt mass used.

Amount of Co Compared to WC Void Space	Preform Processing	Mass of WC Preform (g)	Mass of Co (g)	Co Vol.%	Theoretical Composite Density (g/cm^3)
Lean	Sintered	5.92±0.11	1.78±0.05	35	13.3±0.1
	Un-sintered	5.93±0.12	5.0±0.05	60	11.6±0.1
Exact	Sintered	5.88±0.09	3.55±0.05	51	12.1±0.1
	Un-sintered	5.90±0.08	6.5±0.05	66	11.2±0.1

Macro, Micro, and Optical Image Analysis of Co Infiltrated WC

Fig. 5 shows the macro images of all infiltrated specimens processed with the different parameters. Five specimens were processed for each condition, and it was found that there was consistency in shape and color for all experiments. The specimens infiltrated with un-sintered preforms (Fig. 5a and 5b) did not retain shape; thus, no dimension could be measured to compare to the WC preform. The WC preforms that underwent sintering prior to infiltration (Fig. 5c-d) retained shape better than their un-sintered counterparts (Fig. 5a-b). Specifically, the sintered specimens infiltrated for 1 min with a lean amount of Co retained the cuboid shape except for under the specimens where the cobalt was melted, so the dimensions of the bounding volume can be measured. Furthermore, the sintered specimens infiltrated for 60 min had similar shape retention compared to the sintered specimens infiltrated for 1 min. Thus, it can be deduced that the infiltration time does not have as

much of an effect on the shape retention compared to the amount of sintering of the preform. As a final observation, the color of the specimens processed for 60 min is slightly blue in hue compared to the other specimens due to oxidation from longer time at temperature.

	Exact Co	Lean Co
Un-sintered, 1 min infiltration	A 	B 
Sintered, 1 min infiltration	C 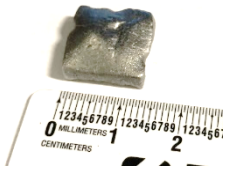	D 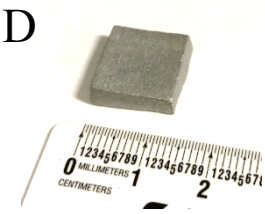
Sintered, 60 min infiltration	E 	F 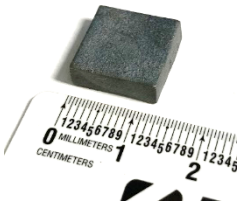

Figure 5: Macro images of all infiltrated WC-Co composites.

Fig. 6 shows optical images of all specimen cross-sections. All specimens are composite of WC-Co, and there appears to be no sections of un-infiltrated WC. All specimens have some residual porosity; however, it can be seen that larger pores are present in the specimens infiltrated with exact amount of Co (Fig. 6a, 6c, and 6e), and this is likely due to higher liquid content trapping more air pockets, more rearrangement of the WC particles in the preform during infiltration, and more solidification shrinkage [22]. Dissolution of WC into the molten Co is evident at the bottom of the specimens that have been sintered prior to infiltration with lean amount of cobalt from the missing material, or "dissolution cavity" in Fig. 6d and 6f. This dissolution cavity is caused by the Co slug progressing through the part at discrete locations, and it is hypothesized that those locations get dissolved and subsequently redistributed during the infiltration because lean specimens do not have any un-infiltrated volume consisting of purely WC preform. Residual porosity in all specimens is likely from processing in an atmosphere and it is hypothesized that infiltrating in a vacuum will reduce the number of pores.

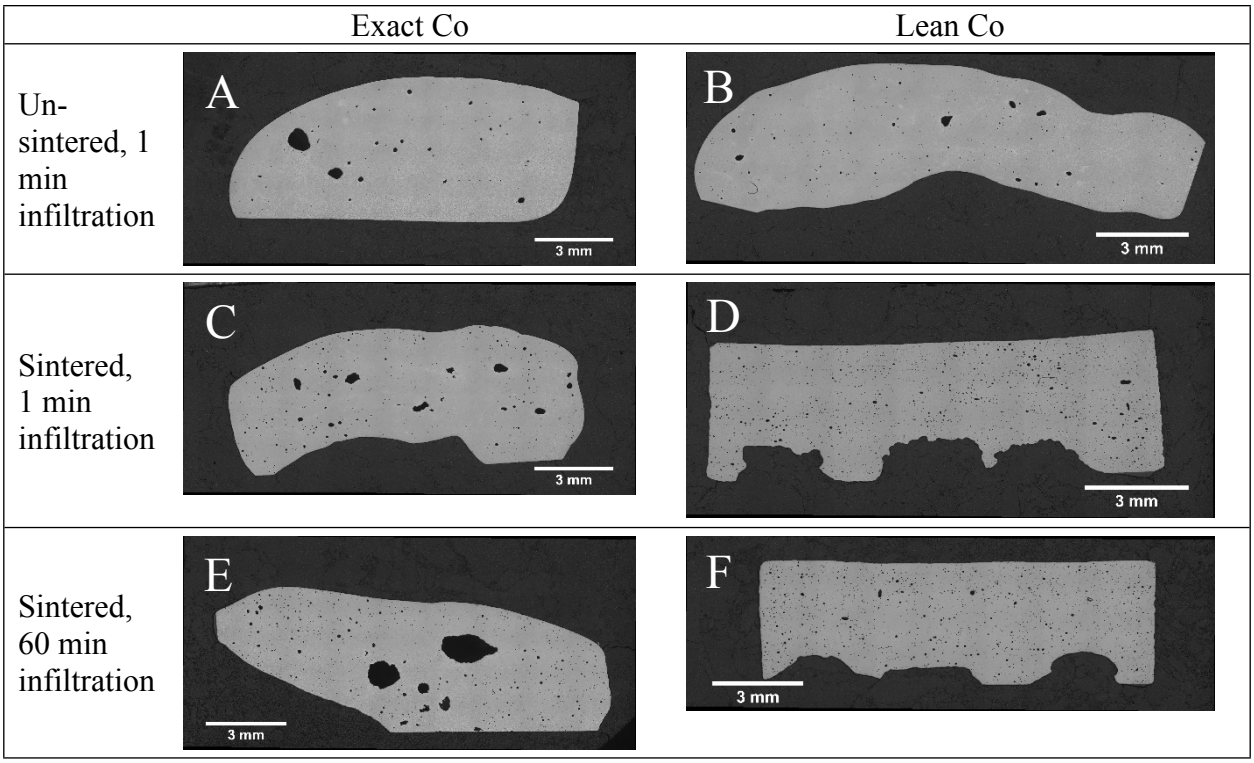

Figure 6: Optical image cross-sections of all infiltrated WC-Co composites.

Fig. 7 shows SEM images of all composite microstructures. All specimens are primarily two phases, the reinforcement (WC) is the lighter grey or white and the metal binder phase (Co) is the darker grey. The SEM images also reveal the amount of WC compared to Co, WC grain size, and WC contiguity. All specimens show that WC has been dissolved since there is faceted WC grain structure in the Co matrix [23]. The grain size is acceptable for applications because our hardness is comparable to WC-Co with similar Co content but smaller grain size, and the grain size in the current research is excellent in wear [24]. There are random agglomerations of WC particles in the specimens with un-sintered preforms, as shown in Fig. 7a-b. The specimens with sintered preforms infiltrated for 1 min (Fig. 7c-d) have more evenly distributed WC and lower amounts of Co compared to their un-sintered counterparts. The specimens with sintered preforms infiltrated for 60 min (Fig. 7e-f) have similar distribution to specimens with sintered preform infiltrated for 1 min but display some grain growth. The differences in skeletal structure in samples with lean Co versus with exact Co comes from the fact that less Co is used to consolidate contributing to microstructures with higher contiguity in lean samples.

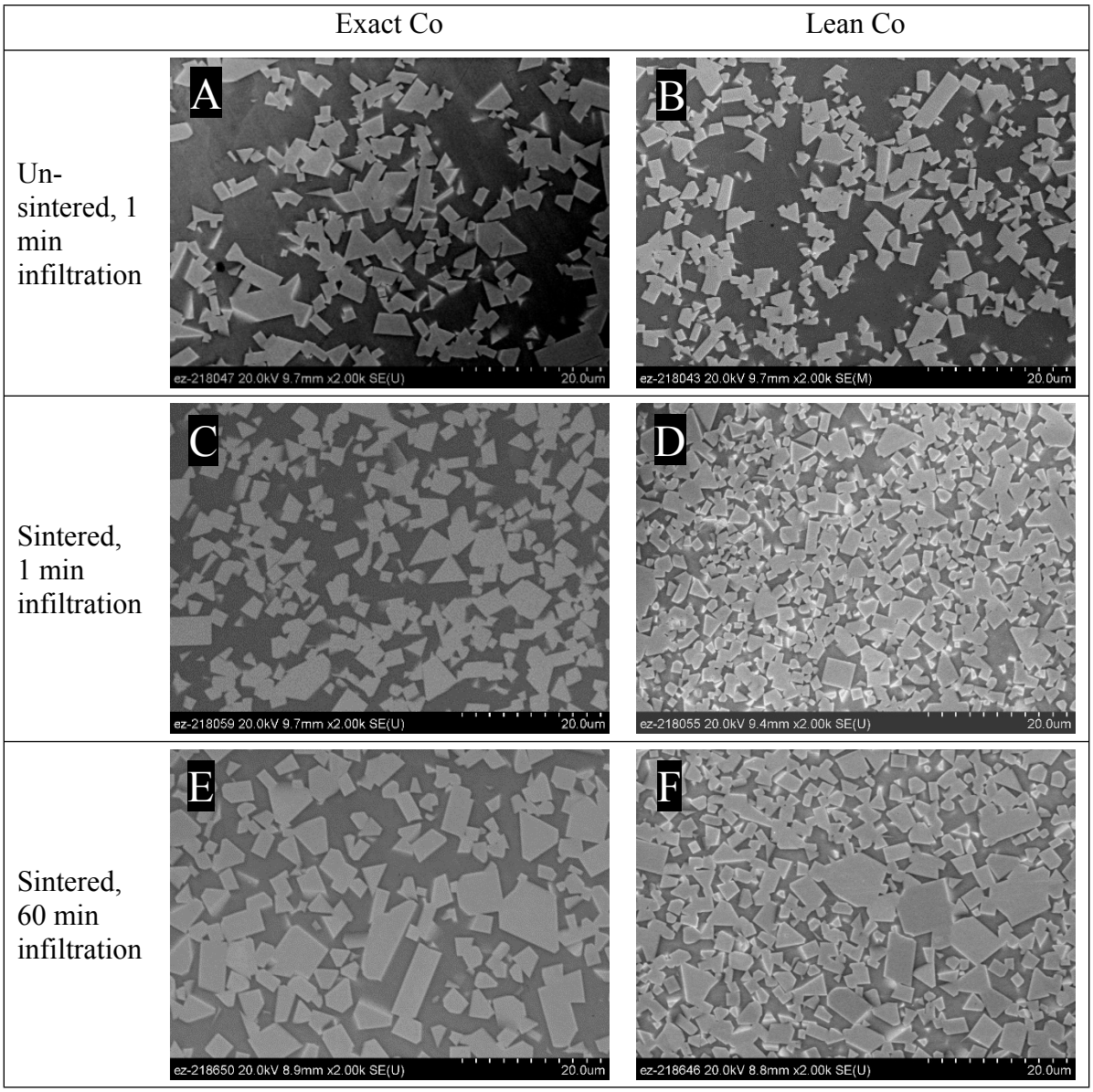

Figure 7: SEM micrographs of all infiltrated WC-Co composites.

Properties

Table 4 shows the physical, mechanical, and dimensional properties of the composite specimens. The Archimedes and areal density measurements are in close agreement as was also shown in other studies with areal density [25]. WC-Co specimen densities are very close to the theoretical values from Table 2, which means near full density, >97%TD, was achieved in the composites. This also means that the areal density technique is valid for WC-Co SEM image cross sections using ImageJ, which is similar to [26]. Processing in a dynamic vacuum may remove the small amount of porosity [27]. Specimen hardness decreased with increasing cobalt content, which is typical in WC-Co. The hardness is slightly lower compared to traditionally-made WC-Co with similar Co content and grain size [28]–[30]. The hardness values of our samples compared to samples printed and sintered with agglomerated powders in [31] are lower because of lower WC content, and there is no data on printed specimens with Co content in the range of the current research. The fracture toughness

of the samples with 32 vol.% Co is 23.2±1.8 MPa·m$^{1/2}$. This is high compared to WC-Co with the same Co content [32], [33], and that is because of small residual pores and the infiltration process. Some grain growth of the WC can be observed in the SEM when comparing Fig. 7c to Fig. 7e and Fig. 7d to Fig. 7f because of more time for the diffusion process in coarsening. Measurable shrinkage is observed in specimens processed with sintered preforms for 1 and 60 min with lean Co. Overall for these composites with sintered WC preforms, there is a total shrinkage from printed to infiltrated of less than 15% and 14% for composites infiltrated for 1 and 60 min, respectively, based on dimensional measurements presented in Table 4. As a result, the lowest vol.% Co achieved is 32, which is in range of 25-37 vol.% Co for applications for high fracture toughness [4]. It is also noted that the un-sintered samples that were subjected to the same heating schedule as the infiltration heating schedule but were not infiltrated showed little to no significant increase in density, meaning that the consolidation during infiltration is solely due to the dissolution, infiltration shrinkage, and redistribution of WC.

Table 4: Physical, mechanical, and dimensional properties of WC-Co composites.

	1 min. Infiltration				60 min. Infiltration	
	Sintered		Un-sintered		Sintered	
	Lean	Exact	Lean	Exact	Lean	Exact
Archimedes Density (g/cm^3, %TD)	13.0, 98.5	12.0, 97.4	11.1, 97.0	10.8, 96.5	12.9, 97.8	11.9, 96.8
Areal Density (g/cm^3, %TD)	13.1,98.7	11.9, 97.3	11.0, 96.8	10.9, 96.7	12.8, 97.6	12.0, 97.0
Actual Vol.% Co	32	48	56	61	34	53
Vickers Hardness (GPa)	9.0±0.2	5.9±0.3	5.8±0.2	4.8±0.2	8.7±0.2	6.6± 0.5
Grain Size (μm)	5.1±2.1	5.0±2.2	5.1±2.1	5.3±2.8	7.2±2.9	7.3±3.2
Fracture Toughness (MPa·m$^{1/2}$)	23.2±1.8	-	-	-	-	-
Final Dimensions (X, Y, Z) (mm)	13.3±0.1, 13.4±0.1, 4.3±0.1	-	-	-	13.3±0.1, 13.4±0.1, 4.3±0.1	-
Total Dimension Change (X, Y, Z) (%)	12, 11, 14	-	-	-	11, 11, 13	-

Fig. 8 shows the XRD patterns of the as-received WC powder and the two sintered preforms infiltrated with lean amounts of Co, one infiltrated for 1 min and the other for 60 min. For the composite specimens with sintered preforms infiltrated for 1 min with lean Co, the phases include WC, face center cubic-Co (fcc-Co), and hexagonal close packed-Co (hcp-Co). η (eta) phase is not detected in the sintered specimen infiltrated for 1 min with lean Co, but it is detected in the sintered specimen infiltrated for 60 min with lean Co. Also, there is an un-identified peak in sintered specimen infiltrated for 1 min with lean Co which could be a contaminant or noise. The composite processed with sintered preform infiltrated for 60 min with lean Co has WC, Co-fcc, Co-hcp, and a small amount of η phase. The presence of η phase in the specimen infiltrated for 60 min is most likely due to the excess time to react and dissolve WC constituents. Finally, it can be observed

from the XRD data that the specimen has higher volume fraction of fcc-Co phase, which is evident from the two extra peaks of fcc-Co at diffraction angles of 19 and 23 degrees compared to the specimen processed for 1 min. This is likely due to longer time at temperature resulting in more WC dissolution. A local scan could be done to determine the un-identified phase and compare small amounts of ternary phase. Limited η phase is wanted because it is brittle and detrimental to mechanical properties. The lack of η phase in this process is most likely due to the 0.2 wt.% excess carbon left behind from the binder burnout, and the process falls within the carbon window [34].

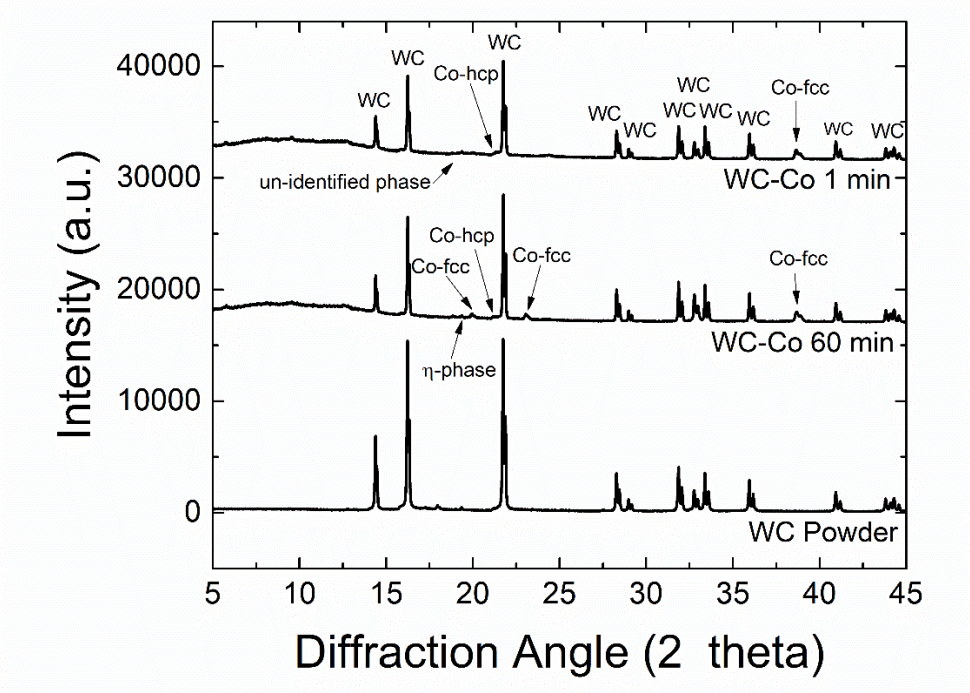

Figure 8: XRD spectra of cermet processed for 1 min, cermet processed for 60 min, and WC powder.

Discussion

Effect of Carbon on Preform Sintering and Composite Microstructure

The process of binder burnout leaves a carbon-rich residue on the particles of 0.2 wt.%, and it is hypothesized that this excess carbon plays a role in both sintering and microstructural evolution. For instance, Figure 4d shows necking of the sintered WC even though sintering of pure WC is typically not achievable at 1600°C without pressure. Most WC powder will have impurities in the form of WO_3 and W_2C, which impedes sintering. It is known that small amounts of carbon can help impure WC powder sintering [35], [36], which is most likely due to the reaction of the excess carbon with the surface impurities to form WC. The excess carbon can reduce surface impurities to form WC that further enhances the neck formation between the powder particles. Excess carbon also aids in limiting η phase that can precipitate upon cooling of the WC-Co composite [37]. Evidence of limited η phase is verified in the XRD scans in Figure 8.

Shaping of WC-Co Specimens Based on Thermodynamics

The shape loss of some of the specimens in this study can be explained by the WC-Co pseudo-binary phase diagram shown in Figure 9. Spots 1-4, which are specimens processed in this paper, are summarized in Table 5. Figure 9 represents these specimens from the current study for their

respective vol.% Co once full infiltration occurs at 1520°C. The amount of liquid in wt.% and vol.% is done using the lever rule for comparison. For the un-sintered specimen infiltrated with exact Co, spot 4 in Figure 9, is purely liquid, or 100% liquid, hence no shape retention. The un-sintered specimen with lean Co, spot 3 in Figure 9, lies close to the liquidus line but in the (WC + liquid) phase. From the lever rule, it is 83 vol.% liquid, hence the poor shape retention. The sintered specimens also lie in the (WC + liquid) phase, so the amount of liquid is calculated for the conditions. The liquid vol.% is 70 for the sintered, exact specimen and 47 for the sintered, lean specimen. It is shown by German (1996) that 30 vol.% liquid is where two-phase mixtures start to behave more like liquids, and the pressed sintering parts will have distortion and slumping. All specimens processed in this paper have higher liquid vol.% than the 30 vol.%, so they display some distortion or slumping. For comparison, the WC-Co that was processed with BJAM by Enneti et al. [15] and sintered does not show slumping like a liquid, but rather only shrinks from liquid-phase sintering. By applying the lever rule to their 12 wt.% Co specimens, they are only 28 vol.% liquid, as shown in Figure 9. Therefore, the shaping behavior in their work does not indicate distortion or slumping, but rather it shows uniform sintering shrinkage in all dimensions. Furthermore, the sintered necks in the present research can help the WC particles retain contiguity and bulk shaping during infiltration as all samples without sintering slumped immensely.

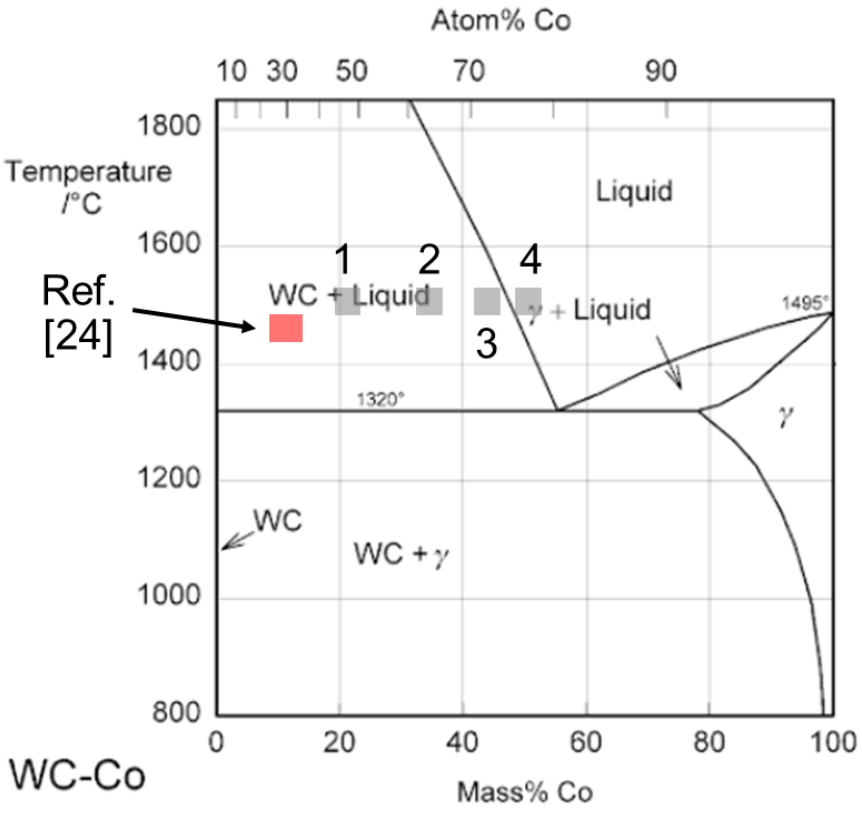

Figure 9: Pseudo-binary phase diagram for WC-Co system [39].

Table 5: Quantifying liquid amount in specimens after infiltration occurs on a WC-Co phase diagram.

Spot on Fig. 9	Conditions	Vol.% Co	Wt.% Co	Wt.% Liquid @ 1520°C by Lever Rule	Vol.% Liquid @ 1520°C by Lever Rule
Ref. [24]	Liquid-phase Sintered, 1 min	19	12	24	28
1	Sintered, Lean, 1 min	32	21	42	47
2	Sintered, Exact, 1 min	48	34	68	70
3	Un-sintered, Lean, 1 min	56	43	86	83
4	Un-sintered, Exact, 1 min	61	49	100	100

Kinetic Considerations

The shape loss from the dissolution cavity and the vol.% Co equilibrium of lean specimens is explained with kinetics of the processing; otherwise, there should be some of the WC that would be un-infiltrated when infiltrating with lean Co, provided no further shrinkage such as liquid phase sintering occurs. Successful fabrication of WC-Co cermets via pressureless melt infiltration depends on two key factors: infiltration kinetics and dissolution kinetics. If the infiltration dominates and occurs faster than the dissolution, it is possible to retain the preform geometry. On the other hand, if dissolution kinetics dominate and are faster than infiltration kinetics, shape loss will likely occur before completion of infiltration while the part starts to slump because of high liquid vol.%. The kinetics of both the infiltration and dissolution are presented hereafter.

The kinetics of infiltration is explained by the Washburn equation to estimate the infiltration time [40]. Eq. (2) summarizes the Washburn equation, where t is the time, h is the height of the capillaries or height of the specimen (assumption for simplicity), ρ is the density of the infiltrating material, r is the radius of the capillaries (assumed to be pore diameter from SEM images of sintered samples), μ is the viscosity of the infiltrating material, γ_{LV} is the surface tension between the infiltrating material and solid preform, θ is the contact angle, and g is the gravitational constant. Based on Eq. (2) and the properties of WC from Table 6, the infiltration time for Co into WC is estimated to be approximately 0.4 s for a 5 mm high WC preform.

$$t = \frac{h^2}{\frac{\rho r^2}{4\mu}\left(\frac{2\gamma_{LV}\cos\theta}{\rho r} - gh\right)} \quad (2)$$

Dissolution kinetics can be modeled using the Noyes-Whitney relationship shown in Eq. (3), where m is the mass, t is the time, A is the surface area of reinforcement material, D is the mixed diffusion coefficient, d is the diffusion distance, C_s is the concentration of saturated solute, and C_b is the initial concentration of solute. These value are found in previous work [41]–[43]. According to Eq. (3) and the properties in Table 6 for the entire preform, dissolution time of the WC in Co reaches saturation in roughly 10 s.

Another kinetic effect is the grain growth, and grains tend to grow exponentially with sintering or processing temperature and time [44], [45]. Fig. 7 and Table 4 show grain growth with increased processing time. The properties between the sintered specimens infiltrated with lean Co are minimal, so the excess time is not need making this method more advantageous for grain size and processing costs and time. Also, the final grain size is very close to the starting average particle size meaning that little grain growth was induced during the entirely of processing the WC-Co composites in the current research.

$$\frac{dm}{dt} = A\frac{D}{d}(C_s - C_b) \quad (3)$$

Table 6: Parameters used in infiltration modeling kinetics.

Parameters for Eq. (2)		Parameters for Eq. (3)	
Height of Specimen, *h*	5 mm	Diffusion coefficient, D	$2\text{x}10^{-9}$ m^2/s
Capillary Radius or Pore Radius, *r*	1 μm	Surface area of powder in preform, A	Specific surface area of powder (0.272 m^2/gm) x 5.9 gm
Co Surface Tension @ 1520°C, γ_{LV}	1.12 J/m^2	Diffusion distance, d	1 nm
Co Density @ 1520°C, ρ	7797 kg/m^3	C_s	0.4 gm
Co Viscosity @ 1520°C, μ	4.543 mPa·s	C_b	0
Contact angle, θ	0 deg. [2]	Diffusion mass, m	5.9 gm

Shaping, Rearrangement, and Vol.% Co Equilibrium

The thermodynamic equilibrium from the phase diagram is not instantaneous and usually requires some time to stabilize, so theoretically, the dissolution can be avoided if processed fast enough. Based on the calculated kinetics of the infiltration, the Co infiltrates almost instantaneously and dissolution reaches a maximum 10 s after. Additionally, based on an ideal furnace cycle, it is possible to process within this timeframe so that the WC parts do not have time to dissolve in Co. However, that was not the case in this study. With the current tube furnace used, the temperature was reached and cooled slowly, so the specimens spent more time at a temperature above the Co melting point, allowing time to equilibrate liquidus phases in the specimens. This temperature was

also consequently much higher than the effective eutectic melting temperature of each specimen, so there was vast slumping in all specimens processed because of high liquid phase content. This dissolution helps to rearrange WC particles to reach the vol.% Co that was targeted in specimens processed with lean Co. In the un-sintered lean specimen, the rearrangement from dissolution of WC allows the WC grains to get closer to each other to reach the vol.% Co without having an un-infiltrated WC preform. This is also likely further aided by the thermodynamics of this specimen because it was 78 wt.% liquid upon infiltration, according to Table 5. In the sintered lean specimen, the rearrangement of WC is evident from the dissolution cavity formed when Co initially is melted and begins to dissolve the WC because that material was completely dissolved at those areas and redistributed elsewhere after infiltration to retain the targeted vol.% Co and leave no part of the WC un-infiltrated. The specimens processed for longer time have very similar attributes to their 1-min counterparts in terms of shaping because they, too, were outside of this dissolution kinetic window, so the only influence was more time for reaction of eta phase and oxidation from the tube furnace.

General Guidelines for This Method

It is shown through analysis of the thermodynamics and kinetics how shaping can be achieved with this process, and this analysis should be done with other composites processed this way. First, the wetting behavior between the two materials must be known or tested. Then, the infiltration can be calculated and experimentally conducted. If the metal infiltrates quickly, dissolution can be considered. If the metal infiltrates slowly and depends on reaction infiltration, the system might benefit from more time, but this encourages more reaction between phases. The amount of metal binder material in the composite is constrained by porosity of the printed preform to obtain near net shaped parts. The lowest amount of infiltration can only be around 15 vol.% if the preform is undergoing sintering because the preform will start to form closed pores above 85%TD. If some pore channels are closed, it would result in incomplete or limited infiltration. The largest amount of infiltration is dependent on the print density of the preform material. For most fracture toughness and hardness applications in cermets, the amount of infiltrant must be around 30 vol.%, which means the density of the printed preform must be around 70%TD if lean amount of Co is not used. Another way to achieve a lower vol.% of infiltrant if the print density is too low is to use a lean amount of infiltrant compared to the void space and allow dissolution to redistribute WC and reach the desired vol.% of Co. In our case, the best shape retention occurs with lean amount of Co. Generally, higher vol.% infiltrant as in MMCs may suffice for wear or even structural applications, but the shaping could be lost with heavy metal infiltration like Co, Ni, and Fe. For WC-Co, the print densities must be higher, the processing should be faster, and a runner may be used to dissolve WC into liquid Co before it reaches the actual WC preform part. Other strategies for improvements in the WC-Co include using higher preform densities and infiltrating with a premade mixture made with Co content corresponding to the eutectic point. Other strategies outside of the WC-Co system include using an infiltrant that dissolves less and coating WC particles in a diffusion barrier material. This method set out on WC-Co can be used for cermets and other MMC systems because of the potential for minimal shrinkage and grain growth.

Conclusion

Nearly fully dense WC-Co composites were achieved by net-shaping WC powder with BJAM and subsequent metal melt infiltration of the specimen with Co with less shrinkage and grain growth compared to other techniques. The optimal vol.% of Co for shape retention in this work is 32

vol.%, which is near the end of the range for high fracture toughness applications. It was found that sintering WC printed preforms prior to infiltration helps maintain the printed geometry by creating necks in the WC powder. Furthermore, using a lean amount of cobalt relative to the amount of void space in the WC preform also improves shape retention due to less liquid content in the specimens at the processing temperature. Theoretical calculations revealed that infiltration happens rapidly because of effective wetting of the two materials, so in typical processing environments, the infiltrated composite is held at temperature for much longer than needed. There was evidence that the necked WC structure is dissolved during processing, allowing for redistribution of the WC particles. Further, the competing kinetics of infiltration and dissolution were discussed. Overall, for specimens that maintained shape, the total shrinkage from printed to infiltrated stages is less than 15%, which is an improvement over other approaches. The grain growth is minimal and is in a range that is useful for many applications. This method of net-shaping a carbide ceramic with BJAM and infiltrating the shape with a metal shows significant promise for WC-Co as well as other cermets and metal matrix composites. This work contributes to the fundamental knowledge in the field of melt-infiltration of AM printed carbides as well as offers an economic solution for shaping carbide-based cermets and metal matrix composites.

Acknowledgments

Corson L. Cramer would like to thank Olivia Shafer for help formatting and editing. This material is based upon work supported by the U.S. Department of Energy, Office of Energy Efficiency and Renewable Energy, Office of Advanced Manufacturing and Propulsion Materials program under the Vehicle Technology Office, under contract number DE-AC05-00OR22725.

References

[1] B. G. Compton and F. W. Zok, "Impact resistance of TiC-based cermets," *Int. J. Impact Eng.*, vol. 62, pp. 75–87, Dec. 2013.

[2] J. Gurland and T. J. Norton, "Role of binder phase in cemented tungsten carbide-cobalt alloys," *Metals (Basel).*, vol. 194, no. 10, pp. 1051–56, 1952.

[3] R. G. Cornwall and R. M. German, "WC-Co enjoys proud history and bright future," *Met. Powder Rep.*, vol. 53, no. 2, pp. 32–36, Feb. 1998.

[4] P. Ettmayer, "HARDMETALS AND CERMETS," *Annu. Rev. Maler. Sci*, vol. 19, pp. 145–54, 1989.

[5] W. Su, Y. Sun, H. Wang, X. Zhang, and J. Ruan, "Preparation and sintering of WC–Co composite powders for coarse grained WC–8Co hardmetals," *Int. J. Refract. Met. Hard Mater.*, vol. 45, pp. 80–85, Jul. 2014.

[6] Z. Baojun, Q. Xuanhui, and T. Ying, "Powder injection molding of WC–8%Co tungsten cemented carbide," *Int. J. Refract. Met. Hard Mater.*, vol. 20, no. 5–6, pp. 389–394, Dec. 2002.

[7] U. Scheithauer, "Droplet-Based Additive Manufacturing of Hard Metal Components by Thermoplastic 3D Printing (T3DP)," *doi.org*, no. 01.

[8] B. D. Kernan, E. M. Sachs, M. A. Oliveira, and M. J. Cima, "Three-dimensional printing of tungsten carbide–10wt% cobalt using a cobalt oxide precursor," *Int. J. Refract. Met. Hard Mater.*, vol. 25, no. 1, pp. 82–94, Jan. 2007.

[9] R. S. Khmyrov, V. A. Safronov, and A. V. Gusarov, "Obtaining Crack-free WC-Co Alloys by Selective Laser Melting," *Phys. Procedia*, vol. 83, pp. 874–881, Jan. 2016.

[10] X. C. Wang, T. Laoui, J. Bonse, J. P. Kruth, B. Lauwers, and L. Froyen, "Direct Selective Laser Sintering of Hard Metal Powders: Experimental Study and Simulation," *Int. J. Adv. Manuf. Technol.*, vol. 19, no. 5, pp. 351–357, Mar. 2002.

[11] H. Kyogoku, T. Uemori, A. Ikuta, K. Yoshikawa, and H. Ohmori, "Direct Selective Laser Sintering of WC-Co Cemented Carbide by Premixing of Additives," in *ASME/ISCIE 2012 International Symposium on Flexible Automation*, 2012, p. 465.

[12] R. S. Khmyrov, V. A. Safronov, and A. V. Gusarov, "Synthesis of Nanostructured WC-Co Hardmetal by Selective Laser Melting," *Procedia IUTAM*, vol. 23, pp. 114–119, Jan. 2017.

[13] B. Berman, "3-D printing: The new industrial revolution," *Bus. Horiz.*, vol. 55, no. 2, pp. 155–162, Mar. 2012.

[14] K. V. Wong and A. Hernandez, "A Review of Additive Manufacturing," *ISRN Mech. Eng.*, vol. 2012, pp. 1–10, Aug. 2012.

[15] R. K. Enneti, K. C. Prough, T. A. Wolfe, A. Klein, N. Studley, and J. L. Trasorras, "Sintering of WC-12%Co processed by binder jet 3D printing (BJ3DP) technology," *Int. J. Refract. Met. Hard Mater.*, vol. 71, pp. 28–35, Feb. 2018.

[16] M. Doyle, K. Agarwal, W. Sealy, and K. Schull, "Effect of Layer Thickness and Orientation on Mechanical Behavior of Binder Jet Stainless Steel 420 + Bronze Parts," *Procedia Manuf.*, vol. 1, pp. 251–262, Jan. 2015.

[17] Z. C. Cordero, D. H. Siddel, W. H. Peter, and A. M. Elliott, "Strengthening of ferrous binder jet 3D printed components through bronze infiltration," *Addit. Manuf.*, vol. 15, pp. 87–92, May 2017.

[18] I. Konyashin *et al.*, "Wettability of tungsten carbide by liquid binders in WC–Co

cemented carbides: Is it complete for all carbon contents?," *Int. J. Refract. Met. Hard Mater.*, vol. 62, pp. 134–148, Jan. 2017.
[19] R. Subramanian and J. . Schneibel, "FeAl–TiC and FeAl–WC composites—melt infiltration processing, microstructure and mechanical properties," *Mater. Sci. Eng. A*, vol. 244, no. 1, pp. 103–112, Mar. 1998.
[20] S. Baklouti, J. Bouaziz, T. Chartier, and J.-F. Baumard, "Binder burnout and evolution of the mechanical strength of dry-pressed ceramics containing poly(vinyl alcohol)," *J. Eur. Ceram. Soc.*, vol. 21, no. 8, pp. 1087–1092, Aug. 2001.
[21] S. Etris *et al.*, "The Application of the Single-Edge Notched Beam to Fracture Toughness Testing of Ceramics," *J. Test. Eval.*, vol. 2, no. 6, p. 503, Nov. 1974.
[22] M. Szweycer and J. Jackowski, "The Reason of Formation of Gas Porosity in Composite Castings with an Aluminum Alloy Matrix," *ISSN Mater. Sci.*, vol. 13, no. 1, pp. 1392–1320, 2007.
[23] Y. J. Park, N. M. Hwang, and D. Y. Yoon, "Abnormal growth of faceted (WC) grains in a (Co) liquid matrix," *Metall. Mater. Trans. A*, vol. 27, no. 9, pp. 2809–2819, Sep. 1996.
[24] I. Konyashin, B. Ries, and F. Lachmann, "Near-nano WC–Co hardmetals: Will they substitute conventional coarse-grained mining grades?," *Int. J. Refract. Met. Hard Mater.*, vol. 28, no. 4, pp. 489–497, Jul. 2010.
[25] C. Grove and D. A. Jerram, "jPOR: An ImageJ macro to quantify total optical porosity from blue-stained thin sections," *Comput. Geosci.*, vol. 37, no. 11, pp. 1850–1859, Nov. 2011.
[26] M. Abdullah, K. K.-I. J. of Physics, and undefined 2009, "A simple method for determining surface porosity based on SEM images using OriginPro software," *ijphysics.com*.
[27] R. Subramanian, J. H. Schneibel, K. B. Alexander, and K. P. Plucknett, "Iron aluminide-titanium carbide composites by pressureless melt infiltration — Microstructure and mechanical properties," *Scr. Mater.*, vol. 35, no. 5, pp. 583–588, Sep. 1996.
[28] Y. . Milman, S. Luyckx, and I. Northrop, "Influence of temperature, grain size and cobalt content on the hardness of WC–Co alloys," *Int. J. Refract. Met. Hard Mater.*, vol. 17, no. 1–3, pp. 39–44, May 1999.
[29] H. Saito, A. Iwabuchi, and T. Shimizu, "Effects of Co content and WC grain size on wear of WC cemented carbide," *Wear*, vol. 261, no. 2, pp. 126–132, Jul. 2006.
[30] K. Jia, T. E. Fischer, and B. Gallois, "Microstructure, hardness and toughness of nanostructured and conventional WC-Co composites," *Nanostructured Mater.*, vol. 10, no. 5, pp. 875–891, Jul. 1998.
[31] R. K. Enneti and K. C. Prough, "Wear properties of sintered WC-12%Co processed via Binder Jet 3D Printing (BJ3DP)," *Int. J. Refract. Met. Hard Mater.*, vol. 78, pp. 228–232, Jan. 2019.
[32] K. S. Ravichandran, "Fracture toughness of two phase WC-Co cermets," *Acta Metall. Mater.*, vol. 42, no. 1, pp. 143–150, Jan. 1994.
[33] J. L. Chermant and F. Osterstock, "Fracture toughness and fracture of WC-Co composites," *J. Mater. Sci.*, vol. 11, no. 10, pp. 1939–1951, Oct. 1976.
[34] C. Liu, "Alternative binder phases for WC cemented carbides," 2014.
[35] A. Nino, K. Takahashi, S. Sugiyama, and H. Taimatsu, "Effects of Carbon Addition on Microstructures and Mechanical Properties of Binderless Tungsten Carbide."
[36] S.-K. Sun *et al.*, "Reactive spark plasma sintering of binderless WC ceramics at 1500 °C,"

Int. J. Refract. Met. Hard Mater., vol. 43, pp. 42–45, Mar. 2014.
[37] C. M. Fernandes and A. M. R. Senos, "Cemented carbide phase diagrams: A review," *Int. J. Refract. Met. Hard Mater.*, vol. 29, no. 4, pp. 405–418, Jul. 2011.
[38] R. M. German, *Sintering theory and practice*. John Wiley & Sons, Inc, 1996.
[39] B. Darvell, *Materials science for dentistry*. 2009.
[40] G. P. Martins, D. L. Olson, and G. R. Edwards, "Modeling of infiltration kinetics for liquid metal processing of composites," *Metall. Trans. B*, vol. 19, no. 1, pp. 95–101, Feb. 1988.
[41] C. Allibert, P. Marty, A. Gagnoud, and Y. Fautrelle, "Estimate of the diffusion coefficient in Co based liquids," *Int. J. Heat Mass Transf.*, vol. 43, no. 3, pp. 437–445, Feb. 2000.
[42] O. O. Eso, P. Fan, and Z. Z. Fang, "A kinetic model for cobalt gradient formation during liquid phase sintering of functionally graded WC–Co," *Int. J. Refract. Met. Hard Mater.*, vol. 26, no. 2, pp. 91–97, Mar. 2008.
[43] M. Walbrühl, "Diffusion in the liquid Co binder of cemented carbides: Ab initio molecular dynamics and DICTRA simulations," 2014.
[44] R. M. German, "Coarsening in Sintering: Grain Shape Distribution, Grain Size Distribution, and Grain Growth Kinetics in Solid-Pore Systems," *Crit. Rev. Solid State Mater. Sci.*, vol. 35, no. 4, pp. 263–305, Nov. 2010.
[45] Y. S. Kwon, G. Son, J. Suh, and K. T. Kim, "Densification and Grain Growth of Porous Alumina Compacts," *J. Am. Ceram. Soc.*, vol. 77, no. 12, pp. 3137–3141, Dec. 1994.